Magnetic response of Sr_2RuO_4: quasi-local spin fluctuations due to Hund's coupling

Hugo Strand, Manuel Zingl, Nils Wentzell, Olivier Parcollet, Antoine Georges

Magnetic response of Sr_2RuO_4: Quasi-local spin fluctuations due to Hund's coupling

Hugo U. R. Strand,[1,*] Manuel Zingl,[1] Nils Wentzell,[1] Olivier Parcollet,[1,2] and Antoine Georges[1,3,4,5]

[1]*Center for Computational Quantum Physics, Flatiron Institute, Simons Foundation, 162 5th Avenue, New York 10010, USA*

[2]*Institut de Physique Théorique (IPhT), CEA, CNRS, UMR 3681, 91191 Gif-sur-Yvette, France*

[3]*Collège de France, 11 place Marcelin Berthelot, 75005 Paris, France*

[4]*Centre de Physique Théorique, Ecole Polytechnique, CNRS, 91128 Palaiseau Cedex, France*

[5]*Department of Quantum Matter Physics, University of Geneva, 24 Quai Ernest-Ansermet, 1211 Geneva 4, Switzerland*

(Received 12 April 2019; revised manuscript received 5 August 2019; published 10 September 2019)

We study the magnetic susceptibility in the normal state of Sr_2RuO_4 using dynamical mean-field theory including dynamical vertex corrections. Besides the well-known incommensurate response, our calculations yield quasi-local spin fluctuations which are broad in momentum and centered around the Γ point, in agreement with recent inelastic neutron-scattering experiments [Steffens *et al.*, Phys. Rev. Lett. **122**, 047004 (2019)]. We show that these quasi-local fluctuations are controlled by the Hund's coupling and account for the dominant contribution to the momentum-integrated response. Although all orbitals contribute equally to the incommensurate response, the enhanced Γ-point response originates from the planar *xy* orbital.

DOI: 10.1103/PhysRevB.100.125120

I. INTRODUCTION

The importance of spin fluctuations for the physics of Sr_2RuO_4 has been emphasized long ago [1]. This material is close to a spin-density-wave instability and small concentrations of impurities trigger ordering [2,3]. Inelastic neutron-scattering (INS) experiments pioneered by Sidis *et al.* [1] and refined over the years [4–10] have revealed that the magnetic response is essentially the sum of: (i) A weakly momentum-dependent contribution centered at Γ (in agreement with the Stoner enhancement factor of the uniform susceptibility by ∼7 as compared to the band value [11,12]) and (ii) a peak at an incommensurate wave-vector $\mathbf{Q}_{\mathrm{SDW}} \approx (0.3, 0.3, 0)$ [13] signaling the proximity to a spin-density-wave (SDW) instability [10]. The peak at $\mathbf{Q}_{\mathrm{SDW}}$ was predicted by Mazin and Singh [14] using density functional theory (DFT) and the random-phase approximation (RPA). However, RPA does not account for the broad structure at Γ, and it predicts that the response at the antiferromagnetic *X* point $\mathbf{Q}_X = (0.5, 0.5, 0)$ is higher than the Γ-point response $\mathbf{Q}_\Gamma = (0, 0, 0)$, in contradiction to experiments [10].

More recently, however, it has been realized that the origin of the strong correlations in this material may not be associated with long-wavelength magnetic correlations but with local correlations driven by Hund's coupling [15,16]. A successful description of an extensive set of physical properties of Sr_2RuO_4 has been obtained following this picture, supported by quantitative dynamical mean-field theory (DMFT) calculations. This includes the large mass enhancements of quasiparticles observed in de Haas–van Alphen experiments [17] and angle-resolved photoemission spectroscopy [18] as well as quasiparticle weights and lifetimes [15], nuclear magnetic resonance [15], optical conductivity [19,20], thermopower [21], Hall coefficient [22], quasiparticle dispersions [23–25], and magnetic response [26–29].

In this paper, we bridge this gap between the spin-fluctuations picture and the Hund's metal picture of the normal state of Sr_2RuO_4 by analyzing the magnetic response function using DMFT. To connect to recent inelastic neutron-scattering experiments [10], we compute the static response as a function of temperature and Hund's coupling, complementing previous DMFT work on the dynamic response [27,29]. Our results reproduce the overall momentum dependence obtained in experiments [10], see Fig. 1, and reveal strong-coupling effects which cannot be accounted for in RPA, such as a suppression of the antiferromagnetic response at $\mathbf{Q}_X$. We find that the response is dominated by quasi-local (weakly

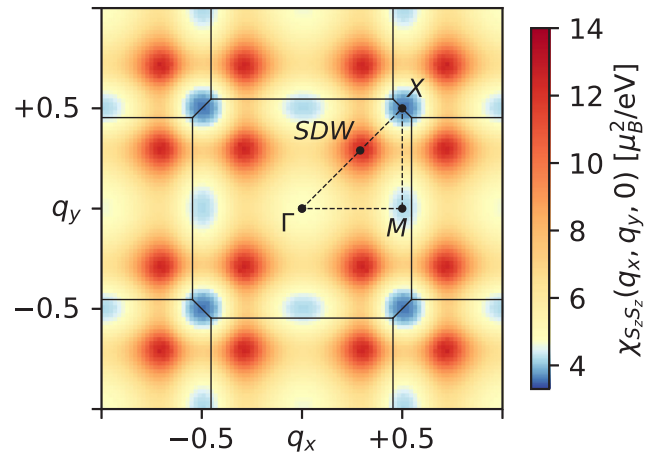

FIG. 1. Spin-susceptibility $\chi_{S_zS_z}(\mathbf{Q})$ from DMFT at $T = 464$ K on the q_x, q_y plane at $q_z = 0$ with incommensurate hot spots at $\mathbf{Q}_{\mathrm{SDW}}$ (red), cold spots at $\mathbf{Q}_M$ and $\mathbf{Q}_X$ (blue), and a broad response centered around $\mathbf{Q}_\Gamma$ (yellow) in units of the reciprocal tetragonal lattice vectors $2\pi/a$ and $2\pi/c$.

*hugo.strand@gmail.com

momentum-dependent) spin fluctuations and show that these fluctuations are controlled by the strength of the Hund's coupling. As discussed at the end of this paper, our findings have direct relevance for theories of the superconducting pairing mechanism, which is still an outstanding and much debated question [30].

II. METHOD

We compute the magnetic susceptibility $\chi_{S_zS_z}(\mathbf{Q})$ using DMFT [31], a DFT derived effective three-band t_{2g} model without spin-orbit coupling [32], and a local Kanamori interaction [33] with Hubbard $U = 2.3$ eV and Hund's $J = 0.4$ eV [15]. The DMFT equations were solved using the hybridization expansion continuous time quantum Monte Carlo [34] implementation in TRIQS [35,36]. The DMFT lattice susceptibility [37–40], first applied to real materials by Park *et al.* [41], is obtained from the DMFT particle-hole irreducible vertex and the Bethe-Salpeter equation (BSE) [31] as implemented in the TRIQS two-particle response function toolbox [42]. For more details see the Appendix. Moreover, the static response at three specific momenta was computed down to much lower temperature, using self-consistent DMFT in applied magnetic fields by zero-field extrapolation in supercells.

III. RESULTS

Figure 1 displays the momentum-dependent magnetic susceptibility from DMFT with hot spots at $\mathbf{Q}_{\mathrm{SDW}}$ and ridges in q_x and q_y connecting these hot spots. This SDW component can be understood from the DFT electronic structure [43] of this material, which has three Ru($4d$)-t_{2g} bands crossing the Fermi level, filled with four electrons. The quasi-two-dimensional γ band, with dominant xy orbital content, has a larger bandwidth (by a factor of $\sim$2) and slightly lower energy than the quasi-one-dimensional α and β bands, originating mainly from the xz and yz orbitals. The peak at $\mathbf{Q}_{\mathrm{SDW}}$ is generated by nesting in the α and β (xz, yz) Fermi-surface sheets, yielding ridges at $(0.3, q_y, 0)$ and $(q_x, 0.3, 0)$ that cross and produce the peak at $\mathbf{Q}_{\mathrm{SDW}}$ [14].

The response in Fig. 1 also shows a large component, broad in momentum, with enhanced intensity centered at Γ in comparison to the cold spots at M and X. This is the signature of the important quasi-local spin fluctuations. Antiferromagnetic fluctuations are suppressed with the X point being the global minimum of the response. This is qualitatively different from the results of weak-coupling approaches, such as RPA [14,44–47]—even when basing RPA on the dressed DMFT Lindhard function [28]—or the fluctuation-exchange approximation [48,49]. In contrast, these approximations yield an enhanced response at the X point and fail to account for the quasi-local response. The latter was not discussed in previous DMFT work [27] but noted in a recent DMFT+GW calculation [29]. Both the quasi-local response and the suppression of the X-point fluctuations are in qualitative agreement with the recent INS experiments [10], see Sec. III C for a more detailed discussion.

Studying the susceptibility along the high-symmetry path Γ-X-M-Γ-Z gives a quantitative picture of the response,

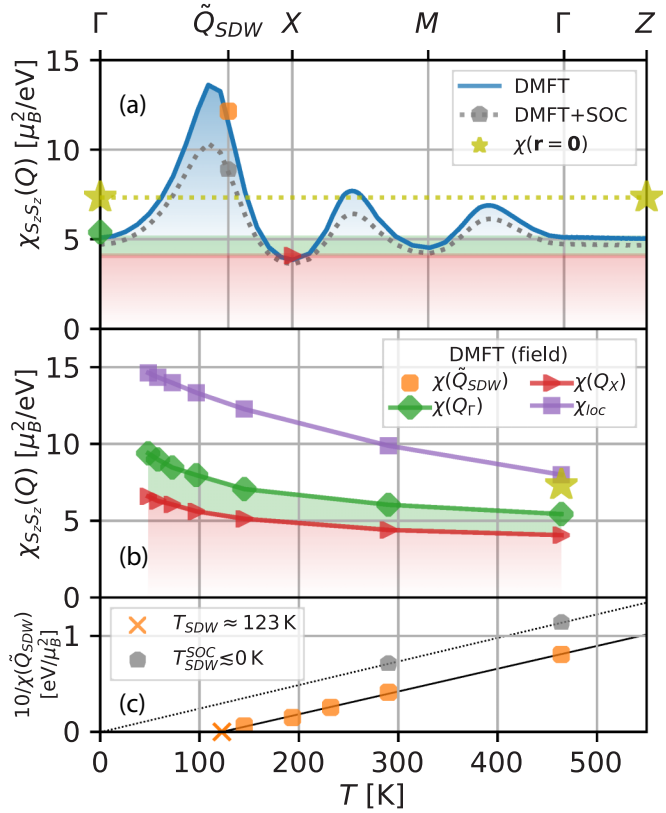

FIG. 2. (a) Spin-susceptibility $\chi_{S_zS_z}(\mathbf{Q})$ from DMFT at $T = 464$ K along the high-symmetry path Γ-X-M-Γ-Z (see Fig. 1) with (gray dotted line) and without (blue line) SOC together with the applied field response at $\mathbf{Q}_\Gamma$ (green diamond), $\mathbf{Q}_X$ (red triangle), $\tilde{\mathbf{Q}}_{\mathrm{SDW}}$ (orange circle), and $\chi(\mathbf{r}=\mathbf{0})$ (yellow star). (b) Temperature dependence of $\chi(\mathbf{Q}_X)$, $\chi(\mathbf{Q}_\Gamma)$, and χ_{loc}. (c) Temperature dependence of $1/\chi(\tilde{\mathbf{Q}}_{\mathrm{SDW}})$ without (circles) and with (pentagon) SOC.

see Fig. 2(a). The incommensurate response at $\mathbf{Q}_{\mathrm{SDW}}$ yields a peak on Γ-X and the nesting ridges, reproduced experimentally in Ref. [8], become local maxima on X-M and M-Γ. The response at $\mathbf{Q}_\Gamma = (0, 0, 0)$ is enhanced relative to the cold spots at $\mathbf{Q}_X = (0.5, 0.5, 0)$ and $\mathbf{Q}_M = (0.5, 0, 0)$ (green-shaded area) with $\mathbf{Q}_X$ being the global minimum. We note in passing that the negligible dispersion on Γ-Z shows that the response is quasi two dimensional. The quasi-local response (red- and green-shaded areas) is the dominant part of the susceptibility, accounting for more than half of the momentum-averaged response (yellow stars).

We also perform complementary calculations of the susceptibility down to much lower temperature through self-consistent DMFT in applied fields at $\mathbf{Q}_\Gamma$, $\mathbf{Q}_X$, and in the vicinity of the incommensurate wave-vector $\mathbf{Q}_{\mathrm{SDW}}$ at $\tilde{\mathbf{Q}}_{\mathrm{SDW}} = (1/3, 1/3, 0)$ (using a $\sqrt{2} \times \sqrt{5}$ three-site supercell), see Figs. 2(b) and 2(c). The result is in quantitative agreement with the DMFT response obtained from the BSE after extrapolating to infinite fermionic frequency cutoff [50], see markers in Fig. 2(a) and the Appendix. This serves as a nontrivial consistency check of our calculations and demonstrates the thermodynamical consistency of DMFT at the two-particle level in a multiorbital model [31,51–53].

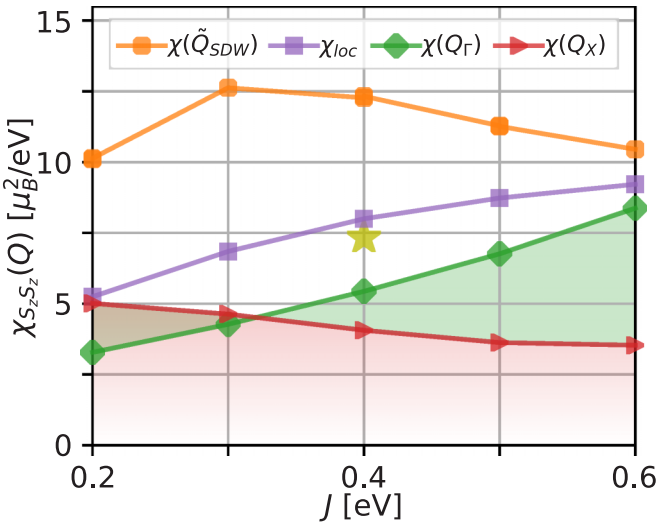

FIG. 3. Spin-susceptibility $\chi_{S_zS_z}(\mathbf{Q})$ for $T = 464$ K from DMFT at $\tilde{\mathbf{Q}}_{\mathrm{SDW}}$ (orange circles), $\mathbf{Q}_\Gamma$ (green diamonds), $\mathbf{Q}_X$ (red triangles), and the impurity local susceptibility χ_{loc} (purple squares) as a function of J at $U = 2.3$ and around $J = 0.4$ eV. The local lattice susceptibility $\chi(\mathbf{r}{=}\mathbf{0})$ (yellow star) is also shown.

When lowering temperature, the spin susceptibility is enhanced, see Fig. 2(b). In particular, both $\chi(\mathbf{Q}_\Gamma)$ and $\chi(\mathbf{Q}_X)$ grow with decreasing temperature, where $\chi(\mathbf{Q}_X)$ can be taken as a direct measure of the background response (red-shaded area). However, the relative Γ-point enhancement (green-shaded area) is robust and roughly constant $\chi(\mathbf{Q}_\Gamma)/\chi(\mathbf{Q}_X) \approx 4/3$ in the studied temperature range. The precise value of this ratio, however, strongly depends on J (see below). The DMFT local impurity susceptibility χ_{loc} shows a similar temperature dependence and is approximately equal to the local susceptibility $\chi(\mathbf{r} = \mathbf{0}) \equiv \frac{1}{V}\sum_{\mathbf{Q}} \chi(\mathbf{Q})$ at $T = 464$ K, see the yellow stars in Figs. 2(b) and 3. Note that when DMFT is applied to finite-dimensional systems χ_{loc} and $\chi(\mathbf{r} = \mathbf{0})$ are, in general, not constrained to be equal. However, the rough agreement strengthens the use of χ_{loc} as a proxy for the momentum average $\chi_{\mathrm{loc}} \sim \chi(\mathbf{r} = \mathbf{0})$ [15,21].

A. Magnetic order and spin-orbit coupling

Although it is known that pristine Sr_2RuO_4 does not order magnetically [12], the question of whether DMFT yields SDW order at low temperature (such as DFT [54]) has not been addressed previously. To answer this question, we make a linear extrapolation of $\chi^{-1}(\tilde{\mathbf{Q}}_{\mathrm{SDW}})$ in temperature, see Fig. 2(c). For the established values of U and J [15], and in the absence of spin-orbit coupling, we find that DMFT yields SDW order at $T_{\mathrm{SDW}} \approx 123$ K, much lower than RPA [55], and compatible with exchange interaction calculations within DFT [54] yielding a Néel temperature of about 200 K [56]. Note, however, that the transition temperature is very sensitive to the precise value of the microscopic parameters, in particular, Hund's coupling J (not shown).

The sensitivity in J raises the question of how the relatively small spin-orbit coupling (SOC) $\lambda_{\mathrm{DFT}} \approx 0.1$ eV [23] affects the ordering temperature. Full DMFT calculations with SOC, in the relevant temperature range, are out of reach with currently available hybridization expansion algorithms. Instead, we resort to an approximate treatment—following Ref. [24]—and add a static self-energy correction to the DMFT bubble in the BSE with a correlation-enhanced SOC coupling $\lambda = 2\lambda_{\mathrm{DFT}}$, see also Ref. [57]. This accounts for the first-order SOC contributions to the DMFT bubble $\chi^{(0)}$ but neglects the effect of SOC on the vertex. Even in this case, our calculations are limited to temperatures at and above room temperature due to a Monte Carlo sign problem, see the Appendix. In momentum space, the magnetic susceptibility with SOC corrections exhibits an overall suppression of the incommensurate and ridge responses whereas the Γ, X, and M points are only weakly affected, see Fig. 2(a). The reduced incommensurate response yields a higher inverse susceptibility, see the two gray pentagons in Fig. 2(c), shifting the magnetic transition to lower temperatures. Using the linear slope of these two points gives approximately $T_{\mathrm{SDW}}^{\mathrm{SOC}} \approx 0$ K. Thus, our tentative conclusion is that a full DMFT+SOC calculation down to low temperatures is likely not to yield SDW ordering. This obviously deserves further study. However, the proximity of the instability to zero temperature is compatible with experiments showing that bulk Sr_2RuO_4 is very close to a magnetic instability [2,3]. Since the inclusion of SOC primarily affects the SDW response, which is not the main focus of our paper, we will neglect it in the following.

B. Signatures of Hund's coupling

To disentangle the microscopic mechanisms driving the different components of the magnetic response, we study their dependence on the Hund's coupling J, see Fig. 3. The incommensurate spin-density-wave response $\chi(\tilde{\mathbf{Q}}_{\mathrm{SDW}})$ displays a nonmonotonic behavior in J, which is an interesting point to be addressed in future studies. Here, we focus on $\mathbf{Q}_\Gamma$ and $\mathbf{Q}_X$ as proxies for the quasi-local response. We note that increasing J suppresses $\chi(\mathbf{Q}_X)$ and drastically increases $\chi(\mathbf{Q}_\Gamma)$ and χ_{loc}. Hence, the Hund's coupling drives the observed Γ-point enhancement [green-shaded area in Figs. 2(a) and 2(b)] as well as the enhancement of the local susceptibility. Since the response around the Γ point is very broad in momentum space (see Fig. 1) this, in turn, suggests that the Hund's coupling is responsible for the overall quasi-local magnetic response. We note in passing that the opposite trends of $\chi(\mathbf{Q}_\Gamma)$ and $\chi(\mathbf{Q}_X)$ as a function of J produces a qualitative change in the magnetic response at $J \sim 0.32$ eV where the two terms cross. We conclude that the Hund's coupling is responsible for the enhanced quasi-local fluctuations and plays a key role in the overall momentum space structure of the magnetic response.

C. Orbital decomposition

We finally investigate how the magnetic response is distributed over the planar xy, out-of-plane xz, and yz orbitals, by studying the decomposition,

$$\chi(\mathbf{Q}) \equiv \chi_{S_zS_z}(\mathbf{Q}) = \sum_{ab} \chi_{S_z^{(a)}S_z^{(b)}}(\mathbf{Q}), \quad a, b \in \{xy, xz, yz\}$$

shown in Fig. 4(a). We find that the orbital-off-diagonal response ($a \neq b$) is roughly 50% of the total magnetic response and confirm [27] that xy, xz, and yz contribute approximately

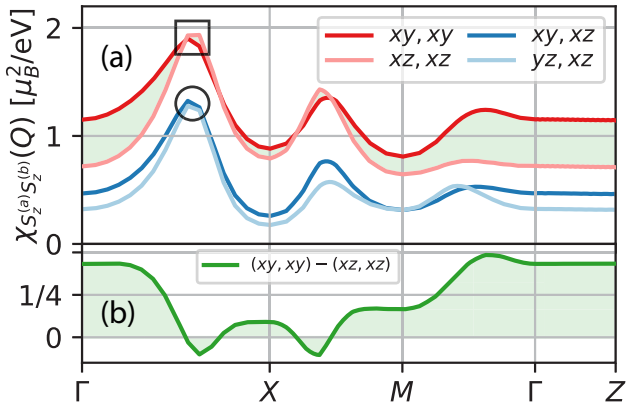

FIG. 4. (a) Orbitally resolved $\chi_{S_z^{(a)}S_z^{(b)}}(\mathbf{Q})$ with $a, b \in \{xy, xz, yz\}$ at $T = 464$ K from DMFT with diagonal xy, xy (red), xz, xz (light red) responses, off-diagonal xy, xz (blue), and yz, xz responses (light blue) which contribute equally at $\mathbf{Q}_{\mathrm{SDW}}$ (black markers). (b) The difference in the diagonal orbital response $(xy, xy) - (xz, xz)$ (green).

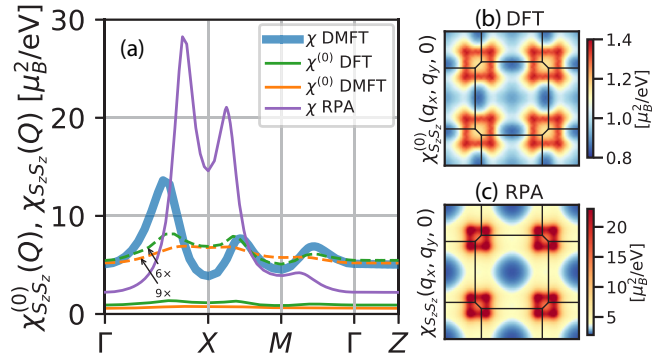

FIG. 5. (a) Spin-susceptibility $\chi_{S_zS_z}(\mathbf{Q})$ at $T = 464$ K on the high-symmetry path Γ-X-M-Γ-Z (see Fig. 1). The DMFT response (blue) is compared to the screened RPA result (purple) and DFT (green) and DMFT (orange) bare bubbles $\chi^{(0)}_{S_zS_z}(\mathbf{Q}) \propto GG$. Note the scaling of the dashed lines. Planar cuts at $q_z = 0$ for (b) DFT and (c) screened RPA are also shown, cf. DMFT in Fig. 1.

equally to the $\mathbf{Q}_{\mathrm{SDW}}$ response, see the markers in Fig. 4(a). Although the $\mathbf{Q}_{\mathrm{SDW}}$ response and the ridges are inherently driven by Fermi-surface nesting, the response is distributed over all orbitals due to the local Kanamori interaction. The interaction couples all orbitals, a feature that is inherited by DMFT vertex function, which, in turn, enters the Bethe-Salpeter equation for the lattice susceptibility, see the Appendix.

Comparing the orbital contributions we find that $\chi_{S_z^{(xy)}S_z^{(xy)}}(\mathbf{Q})$ is markedly higher than $\chi_{S_z^{(xz)}S_z^{(xz)}}(\mathbf{Q})$ around Γ and along M-Γ. It is this part of the $\chi_{S_z^{(xy)}S_z^{(xy)}}(\mathbf{Q})$ response, shown in Fig. 4(b), that is the origin of the broad plateau around Γ and cold spots at X and M in Fig. 1, and the $\mathbf{Q}_\Gamma$ enhancement (green area) in Fig. 2(a). Although this only gives a weak momentum dependence to the large quasi-local magnetic response [red and green areas in Fig. 2(a)], the momentum space variations are extremely sensitive to the Hund's coupling as seen in Fig. 3.

In the recent neutron-scattering experiments, a very broad maximum at Γ has been observed in the spin susceptibility [10]. This feature is not directly visible in our DMFT result at high temperature ($T = 464$ K), see Fig. 1. At this temperature, the incommensurate spin response and the ridges are so thermally broadened that a weak maximum at Γ cannot be observed. However, the orbital-resolved analysis still reveals the broad Γ-centered spectral feature when subtracting the diagonal orbital contributions from the spin susceptibility, see Fig. 4(b).

D. Levels of approximation

We now compare our results to three simpler approximations, (i) the bare bubble, (ii) the DMFT bubble, and (iii) the RPA and show that the DMFT results are the only ones qualitatively compatible with experiments and that the full frequency-dependent vertex is a crucial part of the calculation which cannot be neglected [58]. Indeed, in Fig. 5(a), the DMFT result is compared to the bare DFT and DMFT bubbles ($\chi^{(0)}_{\mathrm{DFT}}$, $\chi^{(0)}_{\mathrm{DMFT}}$) and the screened RPA result χ_{RPA}. The RPA calculation uses—in the spirit of Ref. [28]—the DMFT bubble $\chi^{(0)}$ and screened effective interaction parameters $\tilde{U} = 1.37$ eV and $\tilde{J}/\tilde{U} = 0.4/2.3$, where $\tilde{U}$ has been taken to reproduce the local susceptibility $\chi(\mathbf{r} = \mathbf{0}) \approx 7.3\ \mu_B^2/\mathrm{eV}$ of DMFT. The frequency-dependent particle-hole vertex is clearly essential in the DMFT calculation as $\chi^{(0)}_{\mathrm{DMFT}}$ is much smaller than the DMFT result χ_{DMFT}. $\chi^{(0)}_{\mathrm{DFT}}$ is also strongly suppressed compared to χ_{DMFT}, and the X-point response is higher than both the Γ and the M points [see Fig. 5(b)]. Finally, the screened RPA using the DMFT bubble χ_{RPA} severely overestimates the strength of the nesting peaks, underestimates the constant background response, and fails both to enhance $\chi(\mathbf{Q}_\Gamma)$ and to suppress $\chi(\mathbf{Q}_X)$, see Fig. 5(c).

IV. CONCLUSIONS AND OUTLOOK

In conclusion, we have analyzed the momentum-dependent magnetic response of Sr_2RuO_4 using dynamical mean-field theory, taking full account of vertex corrections. The latter are found to play a crucial role, leading to key effects absent at the RPA level, such as the suppression of the antiferromagnetic response at $\mathbf{Q}_X$. In agreement with neutron-scattering experiments [10], the magnetic response has two main components: a SDW incommensurate response at $\mathbf{Q}_{\mathrm{SDW}}$ and a quasi-local weakly momentum-dependent component, which provides the main contribution to the overall momentum-integrated response. Our main result, on a qualitative level, is the demonstration that the physical origin of the quasi-local magnetic response is the Hund's coupling, hence, reconciling the experimental emphasis put on spin fluctuations in this material with the theoretical picture of Sr_2RuO_4 as a "Hund's metal."

This has far-reaching consequences: Both our theoretical calculations and neutron-scattering experiments indicate that there is no dispersing "quasiferromagnetic" spin-fluctuation mode in Sr_2RuO_4. Hence, pairing mechanisms based on a mediating bosonic mode ("glue") associated with ferromagnetic spin fluctuations [11,12,14,59] have to be seriously reconsidered. The observed suppression of the magnetic response at the X point also invalidates an antiferromagnetic glue. Instead, pairing mechanisms based on a quasi-local mode associated with Hund's coupling offer a promising route. Recent

work has appeared in this direction for model Hamiltonians [60–62] and for iron-based superconductors [63]. However, these mechanisms were proposed in the regime of slow spin fluctuations above the Fermi-liquid temperature and need to be extended to be applicable to Sr_2RuO_4 where the Fermi-liquid temperature is one order of magnitude larger than the superconducting transition temperature. This is a key agenda for future work aiming at solving the 25-year-old puzzle of superconductivity in this material [30].

ACKNOWLEDGMENTS

The authors would like to acknowledge discussions with L. Boehnke, M. Braden, X. Chen, M. Ferrero, A. Georgescu, O. Gingras, S. Hoshino, I. Krivenko, Y. Maeno, I. Mazin, J. Mravlje, R. Nourafkan, T. Schäfer, A. M. Tremblay, P. Werner, and, especially, Y. Sidis. A.G. acknowledges the support from the European Research Council (Grant No. ERC-319286-QMAC). A.G. and H.U.R.S. acknowledge support from the Swiss National Science Foundation (NCCR MARVEL) at the initial stage of this work. The Flatiron Institute is a division of the Simons Foundation.

APPENDIX: TWO-PARTICLE GREEN'S-FUNCTION CALCULATIONS

The DMFT impurity two-particle Green's-function sampling was performed using TRIQS/CTHYB [35,36] and a tailored measurement for the static susceptibility only accumulating the two-particle Green's function for zero bosonic transfer frequency $G^{(2)} \equiv G^{(2)}_{abcd}(\tau, \tau')$,

$$G^{(2)}_{abcd}(\tau,\tau') \equiv \int_0^\beta d\tau_1 d\tau_2 d\tau_3 d\tau_4 \delta(\tau - [\tau_2 - \tau_1]) \times \delta(\tau' - [\tau_4 - \tau_3]) \times \langle \mathcal{T} c^\dagger_a(\tau_1) c_b(\tau_2) c^\dagger_c(\tau_3) c_d(\tau_4)\rangle. \quad \text{(A1)}$$

To measure all components of the two-particle Green's-function $G^{(2)}_{abcd}(\tau, \tau')$ within the CTHYB algorithm [34], we performed a unitary transformation of the single-particle basis to obtain nonzero hybridization functions for all spin-orbital combinations [26]. The transformation produces a sign problem that can—partially—be controlled by tuning the transformation matrix but becomes more severe when lowering temperature, limiting our calculations to room temperature and above ($\beta \leqslant 40\ \mathrm{eV}^{-1}$). Another possibility for sampling these components is the recently developed CTHYB worm sampling [64–69], which we do not apply here.

The two-particle Green's function was directly measured in a product basis of orthogonal polynomials [39] up to order 20 using a total of 8.2×10^8 cycles. For $G^{(2)}(\tau, \tau')$, the discontinuity along the diagonal in imaginary time ($\tau = \tau'$) produces algebraically decaying polynomial coefficients. To alleviate this, we work with the connected two-particle Green's-functions $G^{(2c)}$ related to $G^{(2)}$ by

$$G^{(2)}_{abcd}(\tau,\tau') = G^{(2c)}_{abcd}(\tau,\tau') + G_{ba}(\tau)G_{dc}(\tau') - \int_0^\beta d\bar{\tau}\, G_{da}(\tau' - \bar{\tau})G_{bc}(\tau - \bar{\tau}), \quad \text{(A2)}$$

where $G_{ab}(\tau)$ is the single-particle Green's function and the two last terms on the right-hand side are so-called disconnected contributions to $G^{(2)}$. By evaluating both disconnected contributions in the Legendre polynomial product basis and subtracting them from $G^{(2)}$, we obtain the connected two-particle Green's-function $G^{(2c)}$. Since $G^{(2c)}$ does not have any step discontinuity, the algebraic decay of the polynomial coefficient is one order faster. The procedure enables us to use a lower polynomial order cutoff than in the original algorithm [39]. The noise was further reduced by setting nonsymmetry allowed spin and orbital combinations *abcd* in $G^{(2)}_{abcd}$ explicitly to zero after transforming back to the original basis.

The two-particle response of the impurity is the central quantity required to compute the generalized lattice susceptibility within DMFT. The formalism is well known and has been applied to models from early on [37–40], and, in 2011, it was first applied to real materials within DFT+DMFT by Park *et al.* [41]. The practical procedure is to solve two BSEs in succession. The first equation is the impurity BSE that is used to obtain the DMFT local vertex Γ, and the second BSE is the lattice BSE using the DMFT local vertex to compute the lattice susceptibility.

To solve for the local impurity vertex Γ, the polynomial representation of $G^{(2c)}$ was evaluated in Matsubara frequency space for two different frequency cutoffs $n_\nu = 20$ and 80, and the bare impurity susceptibility $\chi_{0,\mathrm{imp}}$ was constructed directly in frequency space. The impurity Bethe-Salpeter equation for Γ,

$$\Gamma = \chi^{-1}_{0,\mathrm{imp}} - \chi^{-1}_{\mathrm{imp}}, \quad \text{(A3)}$$

where the generalized impurity susceptibility χ_{imp}, given by $\chi_{\mathrm{imp}} = \chi_{0,\mathrm{imp}} + G^{(2c)}$, was then solved for both values of n_ν.

To compute the lattice spin-susceptibility $\chi_{S_zS_z}(\mathbf{q})$, the local DMFT vertex function Γ was used in the lattice Bethe-Salpeter equation for the generalized lattice susceptibility $\chi(\mathbf{q})$,

$$\chi(\mathbf{q}) = [\mathbf{1} - \Gamma\chi_0(\mathbf{q})]^{-1}\chi_0(\mathbf{q}), \quad \text{(A4)}$$

where $\chi_0(\mathbf{q})$ is the bare generalized lattice susceptibility. The spin susceptibility was then computed by tracing out the generalized susceptibility with the spin operators S_z,

$$\chi_{S_z,S_z}(\mathbf{q}) = \sum_{abcd} (S_z)_{ab}\chi_{abcd}(\mathbf{q})(S_z)_{cd}. \quad \text{(A5)}$$

In order to reach quantitative agreement with the susceptibility calculations in applied fields, the lattice spin-susceptibility χ_{S_z,S_z} was computed for both frequency cutoffs $n_\nu = 20$ and 80 and extrapolated to $n_\nu = \infty$ using a linear extrapolation in $1/n_\nu$.

[1] Y. Sidis, M. Braden, P. Bourges, B. Hennion, S. NishiZaki, Y. Maeno, and Y. Mori, Phys. Rev. Lett. **83**, 3320 (1999).

[2] M. Minakata and Y. Maeno, Phys. Rev. B **63**, 180504(R) (2001).

[3] M. Braden, O. Friedt, Y. Sidis, P. Bourges, M. Minakata, and Y. Maeno, Phys. Rev. Lett. **88**, 197002 (2002).

[4] F. Servant, B. Fåk, S. Raymond, J. P. Brison, P. Lejay, and J. Flouquet, Phys. Rev. B **65**, 184511 (2002).

[5] M. Braden, Y. Sidis, P. Bourges, P. Pfeuty, J. Kulda, Z. Mao, and Y. Maeno, Phys. Rev. B **66**, 064522 (2002).

[6] M. Braden, O. Friedt, Y. Sidis, P. Bourges, P. Pfeuty, S. Nakatsuji, Z. Mao, N. Kikugawa, M. Minakata, and Y. Maeno, Physica C **388-389**, 489 (2003).

[7] M. Braden, P. Steffens, Y. Sidis, J. Kulda, P. Bourges, S. Hayden, N. Kikugawa, and Y. Maeno, Phys. Rev. Lett. **92**, 097402 (2004).

[8] K. Iida, M. Kofu, N. Katayama, J. Lee, R. Kajimoto, Y. Inamura, M. Nakamura, M. Arai, Y. Yoshida, M. Fujita, K. Yamada, and S.-H. Lee, Phys. Rev. B **84**, 060402(R) (2011).

[9] K. Iida, J. Lee, M. B. Stone, M. Kofu, Y. Yoshida, and S. Lee, J. Phys. Soc. Jpn. **81**, 124710 (2012).

[10] P. Steffens, Y. Sidis, J. Kulda, Z. Q. Mao, Y. Maeno, I. I. Mazin, and M. Braden, Phys. Rev. Lett. **122**, 047004 (2019).

[11] T. M. Rice and M. Sigrist, J. Phys.: Condens. Matter **7**, L643 (1995).

[12] A. P. Mackenzie and Y. Maeno, Rev. Mod. Phys. **75**, 657 (2003).

[13] In units of the reciprocal tetragonal lattice vectors $2\pi/a$ and $2\pi/c$.

[14] I. I. Mazin and D. J. Singh, Phys. Rev. Lett. **82**, 4324 (1999).

[15] J. Mravlje, M. Aichhorn, T. Miyake, K. Haule, G. Kotliar, and A. Georges, Phys. Rev. Lett. **106**, 096401 (2011).

[16] A. Georges, L. de' Medici, and J. Mravlje, Annu. Rev. Condens. Matter Phys. **4**, 137 (2013).

[17] A. P. Mackenzie, S. R. Julian, A. J. Diver, G. J. McMullan, M. P. Ray, G. G. Lonzarich, Y. Maeno, S. Nishizaki, and T. Fujita, Phys. Rev. Lett. **76**, 3786 (1996); C. Bergemann, S. R. Julian, A. P. Mackenzie, S. NishiZaki, and Y. Maeno, *ibid.* **84**, 2662 (2000); C. Bergemann, A. P. Mackenzie, S. R. Julian, D. Forsythe, and E. Ohmichi, Adv. Phys. **52**, 639 (2003).

[18] A. P. Mackenzie, S.-i. Ikeda, Y. Maeno, T. Fujita, S. R. Julian, and G. G. Lonzarich, J. Phys. Soc. Jpn. **67**, 385 (1998); A. Damascelli, D. H. Lu, K. M. Shen, N. P. Armitage, F. Ronning, D. L. Feng, C. Kim, Z.-X. Shen, T. Kimura, Y. Tokura, Z. Q. Mao, and Y. Maeno, Phys. Rev. Lett. **85**, 5194 (2000); H. Iwasawa, Y. Aiura, T. Saitoh, I. Hase, S. I. Ikeda, Y. Yoshida, H. Bando, M. Higashiguchi, Y. Miura, X. Y. Cui, K. Shimada, H. Namatame, and M. Taniguchi, Phys. Rev. B **72**, 104514 (2005); N. J. C. Ingle, K. M. Shen, F. Baumberger, W. Meevasana, D. H. Lu, Z.-X. Shen, A. Damascelli, S. Nakatsuji, Z. Q. Mao, Y. Maeno, T. Kimura, and Y. Tokura, *ibid.* **72**, 205114 (2005); H. Iwasawa, Y. Yoshida, I. Hase, S. Koikegami, H. Hayashi, J. Jiang, K. Shimada, H. Namatame, M. Taniguchi, and Y. Aiura, Phys. Rev. Lett. **105**, 226406 (2010); H. Iwasawa, Y. Yoshida, I. Hase, K. Shimada, H. Namatame, M. Taniguchi, and Y. Aiura, *ibid.* **109**, 066404 (2012); V. B. Zabolotnyy, D. V. Evtushinsky, A. A. Kordyuk, T. K. Kim, E. Carleschi, B. P. Doyle, R. Fittipaldi, M. Cuoco, A. Vecchione, and S. V. Borisenko, J. Electron. Spectrosc. Relat. Phenom. **191**, 48 (2013); B. Burganov, C. Adamo, A. Mulder, M. Uchida, P. D. C. King, J. W. Harter, D. E. Shai, A. S. Gibbs, A. P. Mackenzie, R. Uecker, M. Bruetzam, M. R. Beasley, C. J. Fennie, D. G. Schlom, and K. M. Shen, Phys. Rev. Lett. **116**, 197003 (2016).

[19] D. Stricker, J. Mravlje, C. Berthod, R. Fittipaldi, A. Vecchione, A. Georges, and D. van der Marel, Phys. Rev. Lett. **113**, 087404 (2014).

[20] X. Deng, K. Haule, and G. Kotliar, Phys. Rev. Lett. **116**, 256401 (2016).

[21] J. Mravlje and A. Georges, Phys. Rev. Lett. **117**, 036401 (2016).

[22] M. Zingl, J. Mravlje, M. Aichhorn, O. Parcollet, and A. Georges, npj Quantum Materials **4**, 35 (2019).

[23] G. Zhang, E. Gorelov, E. Sarvestani, and E. Pavarini, Phys. Rev. Lett. **116**, 106402 (2016).

[24] M. Kim, J. Mravlje, M. Ferrero, O. Parcollet, and A. Georges, Phys. Rev. Lett. **120**, 126401 (2018).

[25] A. Tamai, M. Zingl, E. Rozbicki, E. Cappelli, S. Riccò, A. de la Torre, S. McKeown Walker, F. Y. Bruno, P. D. C. King, W. Meevasana, M. Shi, M. Radović, N. C. Plumb, A. S. Gibbs, A. P. Mackenzie, C. Berthod, H. U. R. Strand, M. Kim, A. Georges, and F. Baumberger, Phys. Rev. X **9**, 021048 (2019).

[26] L. V. Boehnke, Ph.D. thesis, Universität Hamburg, 2015, https://ediss.sub.uni-hamburg.de/volltexte/2015/7325/.

[27] L. Boehnke, P. Werner, and F. Lechermann, Europhys. Lett. **122**, 57001 (2018).

[28] O. Gingras, R. Nourafkan, A.-M. S. Tremblay, and M. Côté, arXiv:1808.02527.

[29] S. Acharya, D. Pashov, C. Weber, H. Park, L. Sponza, and M. van Schilfgaarde, arXiv:1811.05143.

[30] A. P. Mackenzie, T. Scaffidi, C. W. Hicks, and Y. Maeno, npj Quantum Materials **2**, 40 (2017).

[31] A. Georges, G. Kotliar, W. Krauth, and M. J. Rozenberg, Rev. Mod. Phys. **68**, 13 (1996).

[32] The model is identical to the one used in Ref. [25] and derived from a DFT calculation of Sr_2RuO_4 in the experimental structure [70] (at 100 K) using WIEN2K [71] with PBE [72] and 20^3 k points. Maximally localized t_{2g} Wannier functions were constructed using WIEN2WANNIER [73] and WANNIER90 [74–76] (using 20^3 k points and an energy window of $[-2.85, 0.75]$ eV).

[33] J. Kanamori, Prog. Theor. Phys. **30**, 275 (1963).

[34] P. Werner, A. Comanac, L. de' Medici, M. Troyer, and A. J. Millis, Phys. Rev. Lett. **97**, 076405 (2006); P. Werner and A. J. Millis, Phys. Rev. B **74**, 155107 (2006); K. Haule, *ibid.* **75**, 155113 (2007); E. Gull, A. J. Millis, A. I. Lichtenstein, A. N. Rubtsov, M. Troyer, and P. Werner, Rev. Mod. Phys. **83**, 349 (2011).

[35] O. Parcollet, M. Ferrero, T. Ayral, H. Hafermann, I. Krivenko, L. Messio, and P. Seth, Comput. Phys. Commun. **196**, 398 (2015).

[36] P. Seth, I. Krivenko, M. Ferrero, and O. Parcollet, Comput. Phys. Commun. **200**, 274 (2016).

[37] M. Jarrell, Phys. Rev. Lett. **69**, 168 (1992).

[38] J. Kuneš, Phys. Rev. B **83**, 085102 (2011).

[39] L. Boehnke, H. Hafermann, M. Ferrero, F. Lechermann, and O. Parcollet, Phys. Rev. B **84**, 075145 (2011).

[40] N. Lin, E. Gull, and A. J. Millis, Phys. Rev. Lett. **109**, 106401 (2012).

[41] H. Park, K. Haule, and G. Kotliar, Phys. Rev. Lett. **107**, 137007 (2011).

[42] H. U. R. Strand, github.com/TRIQS/tprf (2019), doi:10.5281/zenodo.2638059.

[43] T. Oguchi, Phys. Rev. B **51**, 1385 (1995); D. J. Singh, *ibid.* **52**, 1358 (1995); I. Hase and Y. Nishihara, J. Phys. Soc. Jpn. **65**, 3957 (1996); G. J. McMullan, M. P. Ray, and R. J. Needs, Physica B **223-224**, 529 (1996); P. K. de Boer and R. A. de

Groot, Phys. Rev. B **59**, 9894 (1999); E. Pavarini and I. I. Mazin, *ibid.* **74**, 035115 (2006).
[44] D. K. Morr, P. F. Trautman, and M. J. Graf, Phys. Rev. Lett. **86**, 5978 (2001).
[45] K.-K. Ng and M. Sigrist, J. Phys. Soc. Jpn. **69**, 3764 (2000).
[46] I. Eremin, D. Manske, and K. H. Bennemann, Phys. Rev. B **65**, 220502(R) (2002).
[47] I. Eremin, D. Manske, C. Joas, and K. H. Bennemann, Europhys. Lett. **58**, 871 (2002).
[48] N. Arakawa, Phys. Rev. B **90**, 245103 (2014).
[49] N. Arakawa, Phys. Rev. B **91**, 159906(E) (2015).
[50] D. J. Luitz, Ph.D. thesis, Universtät Würzburg, 2012.
[51] M. Potthoff, Condens. Matter Phys. **9**, 557 (2006).
[52] H. Hafermann, E. G. C. P. van Loon, M. I. Katsnelson, A. I. Lichtenstein, and O. Parcollet, Phys. Rev. B **90**, 235105 (2014).
[53] E. G. C. P. van Loon, H. Hafermann, A. I. Lichtenstein, and M. I. Katsnelson, Phys. Rev. B **92**, 085106 (2015).
[54] B. Kim, S. Khmelevskyi, I. I. Mazin, D. F. Agterberg, and C. Franchini, npj Quantum Materials **2**, 37 (2017).
[55] This is a drastic suppression compared to RPA with bare interactions on the DMFT bubble with $T_{\mathrm{SDW}} \sim 2500$ K and the Hartree-Fock bubble with $T_{\mathrm{SDW}} \sim 6850$ K.
[56] I. I. Mazin (private communication).
[57] G.-Q. Liu, V. N. Antonov, O. Jepsen, and O. K. Andersen., Phys. Rev. Lett. **101**, 026408 (2008).
[58] Note that the central importance of the vertex for obtaining susceptibilities within DMFT is well established; for a recent illustration, see Ref. [77].
[59] I. I. Mazin and D. J. Singh, Phys. Rev. Lett. **79**, 733 (1997).
[60] S. Hoshino and P. Werner, Phys. Rev. Lett. **115**, 247001 (2015).
[61] S. Hoshino and P. Werner, Phys. Rev. B **93**, 155161 (2016).
[62] K. Steiner, S. Hoshino, Y. Nomura, and P. Werner, Phys. Rev. B **94**, 075107 (2016).
[63] T.-H. Lee, A. Chubukov, H. Miao, and G. Kotliar, Phys. Rev. Lett. **121**, 187003 (2018).
[64] P. Gunacker, M. Wallerberger, E. Gull, A. Hausoel, G. Sangiovanni, and K. Held, Phys. Rev. B **92**, 155102 (2015).
[65] P. Gunacker, M. Wallerberger, T. Ribic, A. Hausoel, G. Sangiovanni, and K. Held, Phys. Rev. B **94**, 125153 (2016).
[66] H. Shinaoka, E. Gull, and P. Werner, Comput. Phys. Commun. **215**, 128 (2017).
[67] J. Kaufmann, P. Gunacker, and K. Held, Phys. Rev. B **96**, 035114 (2017).
[68] P. Gunacker, Master's thesis, Technische Universität Wien, Austria, 2014.
[69] P. Gunacker, Ph.D. thesis, Technische Universität Wien, Austria, 2018.
[70] T. Vogt and D. J. Buttrey, Phys. Rev. B **52**, R9843 (1995).
[71] P. Blaha, K. Schwarz, G. K. H. Madsen, D. Kvasnicka, J. Luitz, R. Laskowski, F. Tran, and L. D. Marks, *WIEN2k, An Augmented Plane Wave + Local Orbitals Program for Calculating Crystal Properties* (Karlheinz Schwarz, Technische Universität Wien, Austria, 2018).
[72] J. P. Perdew, K. Burke, and M. Ernzerhof, Phys. Rev. Lett. **77**, 3865 (1996).
[73] J. Kuneš, R. Arita, P. Wissgott, A. Toschi, H. Ikeda, and K. Held, Comput. Phys. Commun. **181**, 1888 (2010).
[74] N. Marzari and D. Vanderbilt, Phys. Rev. B **56**, 12847 (1997).
[75] A. A. Mostofi, J. R. Yates, Y.-S. Lee, I. Souza, D. Vanderbilt, and N. Marzari, Comput. Phys. Commun. **178**, 685 (2008).
[76] N. Marzari, A. A. Mostofi, J. R. Yates, I. Souza, and D. Vanderbilt, Rev. Mod. Phys. **84**, 1419 (2012).
[77] R. Nourafkan, M. Côté, and A.-M. S. Tremblay, Phys. Rev. B **99**, 035161 (2019).